

Linear stability analysis of a sharp-interface model for dewetting thin films

J. R. King · A. Münch · B. A. Wagner

Received: 20 July 2007 / Accepted: 7 August 2008 / Published online: 5 September 2008
© Springer Science+Business Media B.V. 2008

Abstract The stability of the receding front at the growing rim of a thin liquid film dewetting from a substrate is studied. The underlying forces that drive the dewetting motion are given by the intermolecular potential between the liquid film and the substrate. The role of slippage in the emerging instability is studied via a sharp-interface model for the dewetting thin film, which is derived from the lubrication model via matched asymptotic expansions. Using the separation of the time-scale for the slow growth of the rim and the time-scale on which the rim destabilises, the sharp-interface results are compared to earlier results for the lubrication model and good agreement for the unstable modes is obtained. The main advantage of the sharp-interface model is that it allows for the derivation of traveling solutions for the base state and subsequently a systematic linear stability analysis via normal modes. Interestingly, unlike the dispersion relations that are typically encountered for the well-known finger-instability in thin-film flows, where the dependence of the growth rate on the wave number is quadratic, here it is linear.

Keywords Asymptotic methods · High-order nonlinear boundary-value problems · Sharp-interface model · Stability analysis · Thin liquid films

1 Introduction

Contact-line instabilities for thin liquid films that wet a solid substrate have been studied for many decades, both theoretically and experimentally. These instabilities are driven by forces such as, for example, gravity [1–4], Marangoni stresses or both [5–9]. The mathematical modelling of these free-boundary problems often makes use of the fact that the height of the film is small compared to the lateral structures in order to derive dimension-reduced lubrication equations for the film profile $h(x, t)$ from the underlying Navier–Stokes equations in conjunction with conservation of mass, normal and tangential stress boundary conditions at the free boundary $z = h(x, t)$, impermeability and the Navier-slip condition

$$u = bu_z \tag{1.1}$$

J. R. King · A. Münch (✉)
University of Nottingham, Nottingham, UK
e-mail: andreas.muench@nottingham.ac.uk

B. A. Wagner
Weierstrass Institute for Applied Analysis and Stochastics, Berlin, Germany

at the liquid-solid interface, where b is the slip-length parameter, u the lateral velocity and u_z the shear rate. A common assumption in fluid mechanics is the *no-slip* slip condition, i.e., $b = 0$ at the liquid-solid interface $z = 0$. However, this leads to a stress singularity at the moving contact line, which is inherited by the resulting fourth-order lubrication equation for h . To resolve this problem, the equations are regularized for example by allowing $b \neq 0$, with b being orders of magnitude smaller than the height of the actual film, or by prescribing a precursor near the contact line having orders of magnitude smaller height compared to h . Also, one can take the underlying intermolecular potential between the liquid and the substrate into account, which stabilizes a very thin (precursor) film near the contact line, with a thickness close to where the potential has its minimum. The actual choice of regularization near the contact line enters only weakly in the solution as $h \rightarrow 0$ and does not influence the eventual stability dynamics; see for example [1, 9–11].

The thin-film dynamics and its underlying physics is quite different for the case of polymer films of nanoscale thickness that are uniformly spread on a hydrophobically coated substrate. This situation will be considered here. The hydrophobic property is a result of the intermolecular potential between the film and the coated substrate and is composed of repulsive and attractive long-range van der Waals contributions and a short-range term which accounts for Born-type repulsion; see [12, 13]. The latter term provides a cut-off by penalizing a thinning of the film below a positive thickness threshold given by the minimum of the potential. For such a situation the thin polymer film of nanoscopic thickness *feels* the presence of the intermolecular potential and is unstable with respect to small perturbations of the surface h of the film and consequently dewets in a process that is initiated either spontaneously through spinodal decomposition or induced through nucleation. The *dry* spots, or holes, that form as a result, subsequently grow as the newly formed contact line recedes, thereby accumulating liquid in a characteristic capillary rim at the edge of the hole, which increases in width and height as the dewetting proceeds. In several experimental studies it is observed that in some cases the growth of the hole continues until it collides with neighboring holes, while in others the rim bordering the hole destabilizes into finger-like structures that eventually pinch off and form droplets. Such finger-like instabilities have also been observed for straight dewetting fronts instead of radially symmetric fronts, see [14–20].

In addition to these forces that drive the dewetting dynamics, the slip length (or more precisely the *effective* slip length) of liquid polymer films on hydrophobic substrates may be of the same order or even large compared to the film height h ; see for example the review [21]. For these situations, lubrication models that are derived under the assumption of small interfacial slippage compared to the height of the film may not be adequate. For these situations, the impact of interfacial slippage on the dynamics of the dewetting film has been discussed by several authors, both experimentally and theoretically [22–26]. On the theoretical side this problem was addressed by investigating the possible asymptotic balances of the underlying free-boundary problem for increasing order of magnitude of the slip length b and deriving closed form dimension-reduced lubrication models for each of the relevant regimes. In particular, we identified two *distinguished limits*. One of them is the so-called *weak-slip* model

$$h_t = - (M(h) (h_{xx} - \phi'(h))_x)_x, \quad (1.2)$$

where $M(h) = h^3 + b h^2$ and the slip-length parameter b is smaller than h . While this model is the well-known lubrication model regularized via an appropriate intermolecular potential ϕ , the second distinguished limit, the *strong-slip* model

$$\text{Re} (u_t + uu_x) = \frac{4}{h} (hu_x)_x + (h_{xx} - \phi'(h))_x - \frac{u}{\beta_s h}, \quad (1.3a)$$

$$h_t = - (hu)_x \quad (1.3b)$$

was new. Here, $u(x, t)$ denotes the velocity in the lateral direction. The slip-length parameters b and β_s are related by orders of magnitude via $b \sim \beta_s / \nu^2$, and $0 < \nu \ll 1$ refers to the lubrication scaling, i.e., the vertical to lateral-scale separation of the thin film. The new terms $\text{Re} (u_t + uu_x)$, with Re denoting the Reynolds number, and $(4/h)(hu_x)_x$ are the inertial and Trouton viscosity terms, respectively. The derivative $\phi'(h)$ of the intermolecular potential denotes the disjoining pressure, which we write in the scaled form [12]

$$\phi'(h) = \varepsilon^{-1} \Phi'(h/\varepsilon), \quad \text{where } \Phi(h) = \frac{1}{8h^8} - \frac{1}{2h^2}, \quad (1.4)$$

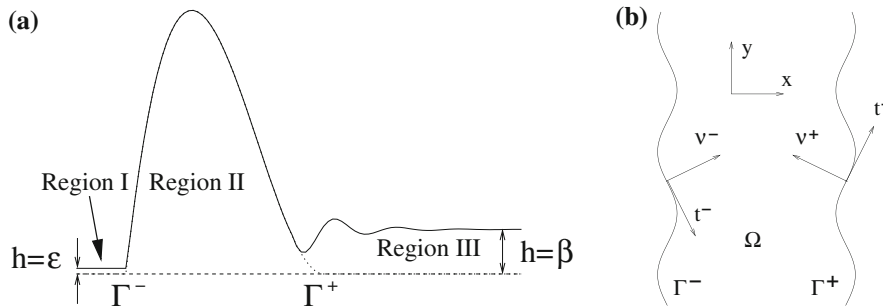


Fig. 1 (a) Sketch of a cross-section of a dewetting rim. (b) Sketch of a top view of a (perturbed) ridge for a sharp-interface model, showing the domain Ω occupied by the ridge and the two free-boundary curves Γ^\pm

so that the minimum at $h = \epsilon \ll 1$ of ϕ occurs at $h = \epsilon$, i.e., very thin films with a thickness scale of ϵ are energetically preferred to thicker films, which therefore tend to dewet.

Additionally, the weak-slip and the strong-slip models contain as limiting cases three further lubrication models. One of which is the already mentioned no-slip model which is obtained when $b = 0$ in the weak-slip model. The second one is obtained from the strong-slip model in the limit $\beta_s \rightarrow \infty$ and describes the dynamics of suspended free films; see e.g. [27, 28]. The third limiting case derived in [24] has orders of magnitude for the slip-length parameter β_I/v^α lying in between those that lead to the weak and the strong-slip model, i.e., $0 < \alpha < 2$. The corresponding *intermediate-slip* model is given by

$$h_t = - \left(h^2 (h_{xx} - \phi'(h))_x \right)_x. \tag{1.5}$$

This model and its dynamical properties is the focus of this study. We note first that within the physical context described above, the dewetting rates of traveling-wave solutions for the above family of lubrication models have been investigated using matched asymptotic expansions and numerical solutions [24, 29]. Interestingly, while for small and very large slip lengths the dewetting rates turn out to be nearly constant with logarithmic corrections, the intermediate-slip model (1.5) shows the distinct property of having dewetting rates proportional to $t^{-1/3}$. These results confirmed earlier results by [30–32], where the dewetting rate and shape of the rim has been discussed using approximate formulas derived from scaling arguments and energy balances. Within another context, where lubrication models with mobility h^n where considered, the dewetting rates for the cases of h^3 (no-slip) and h^2 (intermediate-slip) were also derived using matched asymptotic expansions by [33].

In [23] a linear stability analysis showed that small perturbations of the receding front are amplified, but in the intermediate-slip case by orders of magnitude larger than in the no-slip case. More significantly, while the perturbations become symmetrical in the no-slip case, they are asymmetrical in the intermediate-slip case and in [34] it was shown that these properties carry over into the nonlinear regime of the lubrication models. These results confirmed earlier experiments and heuristic arguments in [25] where it was proposed that for the dewetting rate $t^{-1/3}$ the receding and growing rim slows down, which in turn enforces any perturbations that divide the rim in thicker and thinner parts along the direction of the contact line.

The problem of the stability analysis of the lubrication models for dewetting films is that the base state is time-dependent and so the interval of unstable and stable wavelengths shifts in time. This makes the analysis much more difficult and the direct numerical study of the stability problem becomes rather time-consuming. However, at the onset of the instability the height of the rim is much larger than the height (ϵ) of the residual film and the height (β) of the undisturbed film; see the sketch in Fig. 1. This opens the possibility to reduce the stability problem to the problem of a rim with appropriate boundary conditions obtained by asymptotic matching of the three regions, and we call the resulting model the *sharp-interface model*. At the same time this asymptotic analysis will separate the slow growth of the rim from the faster time-scale on which the contact line destabilizes. As a result, the linear stability analysis can be reduced to an eigenvalue analysis and hence opens up the possibility of obtaining results on the effective wavelengths more easily, for comparison with physical experiments.

We begin our study by first deriving the sharp-interface model in Sect. 2. Then we first derive the traveling wave solutions in Sect. 3 and study their stability in Sect. 4. Finally we compare our results to those for the full lubrication model studied in [23, 34].

2 Derivation of the sharp-interface model

2.1 Outer problem

For the stability analysis of the contact line we consider the two-dimensional lubrication model for the intermediate-slip case

$$h_t + \nabla \cdot \left[h^2 \nabla \cdot \left(\Delta h - \varepsilon_1^{-1} \Phi' (h/\varepsilon_1) \right) \right] = 0 \tag{2.1}$$

and far-field conditions

$$\lim_{x \rightarrow -\infty} h(x, y, t) = \varepsilon_1, \quad \text{and} \quad \lim_{x \rightarrow +\infty} h(x, y, t) = 1, \tag{2.2}$$

where $\varepsilon_1 \ll 1$. This formulation is convenient, for example, for numerical simulations, where the unperturbed film thickness is held fixed and the growth of the rim is observed. For the derivation of the sharp-interface model, it is important that both the residual film on the left and the unperturbed film on the right are much smaller in height of than the actual rim. Therefore, we rescale the film profile h by a quantity $1/\beta$ that is large compared to the unperturbed film thickness, i.e., $\beta \ll 1$, but at most of the order of the typical ridge height. To maintain the form of the governing equation and the potential, the other variables are scaled accordingly, i.e.,

$$h = \frac{1}{\beta} \tilde{h}, \quad x = \frac{1}{\beta} \tilde{x}, \quad y = \frac{1}{\beta} \tilde{y}, \quad t = \frac{1}{\beta^2} \tilde{t}. \tag{2.3}$$

Introducing these scalings yields, after dropping \sim 's,

$$h_t + \nabla \cdot \left[h^2 \nabla \cdot \left(\Delta h - \varepsilon^{-1} \Phi' (h/\varepsilon) \right) \right] = 0 \tag{2.4}$$

and far-field conditions

$$\lim_{x \rightarrow -\infty} h(x, y, t) = \varepsilon, \quad \text{and} \quad \lim_{x \rightarrow +\infty} h(x, y, t) = \beta, \tag{2.5}$$

where $\varepsilon \equiv \varepsilon_1 \beta \ll \beta \ll 1$. This is the appropriate outer scaling for the subsequent derivations.

2.2 Transformation to inner coordinates near the contact line

Let $\mathbf{x} = (x, y)$ be a point in the neighborhood of the contact line Γ^- , parametrized by $\mathbf{r}^-(t, s) = (r_1^-(t, s), r_2^-(t, s))$, where s denotes arclength. Then

$$\mathbf{x} = \mathbf{r}^-(t, s) + \varepsilon \chi \mathbf{v}(t, s) \tag{2.6}$$

defines the boundary layer with χ being the boundary-layer or ‘inner’ variable. The normal $\mathbf{v}(t, s) = (-r_{2s}^-(t, s), r_{1s}^-(t, s))$ and the tangential unit vector $\mathbf{t}(t, s) = (r_{1s}^-(t, s), r_{2s}^-(t, s))$ are chosen so that (\mathbf{t}, \mathbf{v}) is a right-hand system and \mathbf{v} points into the ridge; i.e., into Ω ; see Fig. 1(b). In the inner region the height is much smaller and we set

$$h = \varepsilon v. \tag{2.7}$$

Making use of Appendix A in [35], we obtain the expression

$$\begin{aligned} \nabla \cdot \left(h^2 \nabla p \right) = \varepsilon^2 \left[2v \left(r_{1s}^-(1 - \varepsilon \chi \kappa) v_s + \varepsilon^{-1} r_{2s}^- v_\chi \right) \left(r_{1s}^-(1 - \varepsilon \chi \kappa) p_s + \varepsilon^{-1} r_{2s}^- p_\chi \right) \right. \\ \left. + 2v \left(r_{2s}^-(1 - \varepsilon \chi \kappa) v_s - \varepsilon^{-1} r_{1s}^- v_\chi \right) \left(r_{2s}^-(1 - \varepsilon \chi \kappa) p_s - \varepsilon^{-1} r_{1s}^- p_\chi \right) \right. \\ \left. + v^2 \left(\varepsilon^{-2} p_{\chi\chi} + \varepsilon^{-1} \kappa p_\chi + p_{ss} - \chi \kappa^2 p_\chi \right) \right], \end{aligned} \tag{2.8}$$

where

$$p = -\varepsilon^{-1} (v_{\chi\chi} - \Phi'(v)) - \kappa v_\chi - \varepsilon (v_{ss} - \chi\kappa^2 v_\chi). \tag{2.9}$$

Hence, to leading order in ε , the second term of (2.4) is

$$\nabla \cdot (h^2 \nabla p) \sim \varepsilon^{-1} \left[v^2 (v_\chi - \Phi'(v)) \right]_\chi. \tag{2.10}$$

Since the first term of (2.4) is transformed to

$$h_t = -\varepsilon V^t (1 - \varepsilon z \kappa) v_s + V^v v_z + \varepsilon v_t, \tag{2.11}$$

the leading-order inner problem becomes

$$\left[v^2 (v_{\chi\chi} - \Phi'(v)) \right]_\chi = 0, \tag{2.12}$$

together with the boundary conditions

$$\lim_{\chi \rightarrow -\infty} v = 1, \quad \lim_{\chi \rightarrow -\infty} v_\chi = 0, \quad \lim_{\chi \rightarrow -\infty} v_{\chi\chi} = 0. \tag{2.13}$$

Integrating (2.13) twice, using the fact that the potential satisfies $\Phi'(1) = 0$ since Φ has a minimum there, we get $v_{\chi\chi} = \Phi'(v)$, whence

$$v_\chi = 2^{1/2} (\Phi(v) - \Phi(1))^{1/2}. \tag{2.14}$$

For matching we need the behavior for large χ , which is

$$v_\chi \rightarrow 2^{1/2} (-\Phi(1))^{1/2} \equiv \lambda \quad \text{as } \chi \rightarrow \infty. \tag{2.15}$$

Transformation back to outer variables via

$$v = \chi\lambda, \quad \text{where } \chi = \frac{(\mathbf{x} - \mathbf{r}) \cdot \mathbf{v}}{\varepsilon}$$

yields

$$h = (\mathbf{x} - \mathbf{r}) \cdot \mathbf{v} \lambda. \tag{2.16}$$

The sharp-interface model then results from the leading-order outer problem, together with the boundary condition found by matching to (2.16),

$$h_t = -\nabla \cdot (h^2 \nabla \Delta h), \quad \text{in } \Omega, \tag{2.17}$$

$$\frac{\partial h}{\partial \mathbf{v}} = \lambda, \quad h = 0, \quad h \frac{\partial}{\partial \mathbf{v}} \Delta h - V_v^- = 0 \quad \text{on } \Gamma^-, \tag{2.18}$$

where the third boundary condition in (2.18) arises by letting $\chi \rightarrow \infty, v \rightarrow \infty$ in (2.12). In (2.18), we have introduced the notation

$$V_v^- \equiv \mathbf{r}_t^- \cdot \mathbf{v}. \tag{2.19}$$

Next, we derive the boundary condition on Γ^+ .

2.3 Transformation to inner coordinates near the undisturbed film

Here we let $\mathbf{x} = (x, y)$ be a point in the neighborhood of the sharp interface Γ^+ , parametrized by $\mathbf{r}^+(t, s) = (r_1^+(t, s), r_2^+(t, s))$. Then

$$\mathbf{x} = \mathbf{r}^+(t, s) + \beta^\gamma \zeta \mathbf{v}(t, s) \tag{2.20}$$

defines the boundary layer with ζ being the ‘inner’ variable, where the scaling exponent γ remains to be determined. As before, the normal unit vector $\mathbf{v}(t, s) = (-r_{2s}^+(t, s), r_{1s}^+(t, s))$ points into ridge (Fig. 1(b)) and the tangential unit vector $\mathbf{t}(t, s) = (r_{1s}^+(t, s), r_{2s}^+(t, s))$ is chosen so that (\mathbf{t}, \mathbf{v}) form a right-hand system.

In this second inner region we set

$$h = \beta u. \quad (2.21)$$

To leading order in β we find for h_t the expression

$$h_t \sim -\beta^{1-\gamma} V^v u_\zeta \sim -\beta^{1-\gamma} (\mathbf{r}_t^+ \cdot \mathbf{v}) u_\zeta \quad (2.22)$$

and we have

$$\nabla \cdot \left(h^2 \nabla \left(\Delta - \varepsilon^{-1} \Phi(h/\varepsilon) \right) \right) \sim \beta^{3-4\gamma} \left(u^2 \left(u_{\zeta\zeta} - \beta^{2\gamma-1} \varepsilon^{-1} \Phi(\beta u/\varepsilon) \right)_\zeta \right)_\zeta. \quad (2.23)$$

A traveling-wave balance for the moving rim thus requires

$$\gamma = \frac{2}{3}. \quad (2.24)$$

In order for the intermolecular forces to play no role in this region we require

$$O\left(\beta^{2\gamma-1} \varepsilon^{-1} \Phi(\beta u/\varepsilon)\right) \ll 1, \quad (2.25)$$

which introduces a restriction on β in terms of ε , namely $\varepsilon^2 \ll \beta^{8/3}$. Hence, we obtain for the leading-order inner problem near the undisturbed film

$$-V_v^+(s, t) u_\zeta + \left(u^2 u_{\zeta\zeta\zeta} \right)_\zeta = 0, \quad (2.26)$$

where

$$V_v^+(s, t) \equiv \mathbf{r}_t^+ \cdot \mathbf{v}. \quad (2.27)$$

This we integrate with respect to ζ and use the far-field condition

$$\lim_{\zeta \rightarrow -\infty} u = 1 \quad (2.28)$$

to obtain

$$-V_v^+(s, t) (u - 1) + u^2 u_{\zeta\zeta\zeta} = 0. \quad (2.29)$$

For the matching to the outer problem we rescale first $\zeta = \eta / (-V_v^+)^{1/3}$ to obtain the equation

$$u_{\eta\eta\eta} = \frac{u - 1}{u^2}. \quad (2.30)$$

See for example [36], where this equation has been discussed. Note that, we can assume that, as long as the basic motion of the rim in outer coordinates is to the right (i.e., in the positive direction of the x -axis), $V_v^+(s, t)$ is *negative*; hence the orientation is not reversed by the rescaling from ζ into η variables. Therefore, the flat-film far-field condition and the matching conditions are imposed at $\eta \rightarrow -\infty$ and $\eta \rightarrow +\infty$, as before. Equation (2.30) has a solution with leading-order behavior

$$u(\eta) \sim 2(2/3)^{1/2} \eta^{3/2} \quad \text{as } \eta \rightarrow +\infty \quad (2.31)$$

and hence

$$u(\zeta) \sim 2(2/3)^{1/2} (-V_v^+)^{1/2} \zeta^{3/2} \quad (2.32)$$

as $\zeta \rightarrow \infty$. In outer scales we obtain

$$h = 2(2/3)^{1/2} (-V_v^+)^{1/2} ((\mathbf{x} - \mathbf{r}^+) \cdot \mathbf{v})^{3/2} \quad (2.33)$$

as the appropriate matching condition.

Finally we get for the sharp-interface model

$$h_t = -\nabla \cdot (h^2 \nabla \Delta h), \quad \text{in } \Omega, \tag{2.34a}$$

$$h = 0, \quad \frac{\partial h}{\partial \mathbf{v}} = \lambda, \quad h \frac{\partial}{\partial \mathbf{v}} \Delta h - V_v^- = 0 \quad \text{on } \Gamma^-, \tag{2.34b}$$

$$h \sim 2(2/3)^{1/2} (-V_v^+)^{1/2} ((\mathbf{r}^+ - \mathbf{x}) \cdot \mathbf{v})^{3/2} \quad \text{as } x \rightarrow \mathbf{r}^+. \tag{2.34c}$$

For the subsequent discussion of the sharp-interface model it is convenient to introduce the parametrization of Γ^- and Γ^+ as graphs of functions of $s^-(y, t)$ and $s^+(y, t)$, i.e., $y \mapsto (-y, -s^-(y, t))$ and $y \mapsto (y, s^+(y, t))$, respectively. We obtain the following expressions for the tangent and normal unit vectors

$$\mathbf{t}^- = \frac{(-s_y^-, -1)}{\sqrt{(s_y^-)^2 + 1}} \quad \text{and} \quad \mathbf{v}^- = \frac{(1, -s_y^-)}{\sqrt{(s_y^-)^2 + 1}} \tag{2.35}$$

on Γ^- , and

$$\mathbf{t}^+ = \frac{(s_y^+, 1)}{\sqrt{(s_y^+)^2 + 1}} \quad \text{and} \quad \mathbf{v}^+ = \frac{(-1, s_y^+)}{\sqrt{(s_y^+)^2 + 1}} \tag{2.36}$$

on Γ^+ .

3 Traveling-wave solutions

We now assume that the base state is a traveling wave that moves with constant speed c and does not depend on y . The ansatz is $h = h_0(\bar{x})$, where $\bar{x} = x - ct$, and $\bar{s}_0^\pm = s_0^\pm - ct$, with constant \bar{s}_0^\pm (i.e., independent of \bar{x} , y or t). Inserting the new variables, we obtain, after dropping the bars,

$$h_0 h_{0xxx} = c, \tag{3.1a}$$

$$h_0 = 0, \quad h_{0x} = \lambda, \quad h_0^2 h_{0xxx} = 0 \quad \text{on } x = s_0^-, \tag{3.1b}$$

$$h_0 \sim 2(2/3)^{1/2} c^{1/2} (s_0^+ - x)^{3/2} \quad \text{for } x \rightarrow s_0^+. \tag{3.1c}$$

Here we have integrated the resulting ODE once and used the boundary conditions to fix the constant of integration.

We can rescale (3.1a–3.1c) to eliminate c and λ via

$$h_0 = (\lambda^3/c)\varphi_0, \quad x = (\lambda^2/c)\xi + s_0^-, \quad s_0^+ = (\lambda^2/c)d + s_0^-, \tag{3.2}$$

which yields (with $' = d/d\xi$):

$$\varphi_0 \varphi_0''' = 1, \tag{3.3a}$$

$$\varphi_0 = 0, \quad \varphi_0' = 1, \quad \varphi_0^2 \varphi_0''' = 0 \quad \text{on } \xi = 0, \tag{3.3b}$$

$$\varphi_0 \sim 2(2/3)^{1/2} (d - \xi)^{3/2} \quad \text{for } \xi \rightarrow d. \tag{3.3c}$$

Note that this can be integrated to

$$\varphi_0 \varphi_0'' - \frac{1}{2} \varphi_0^2 = \xi - d. \tag{3.4}$$

We now discuss solutions of (3.3). Note first that the function on the right-hand side of (3.3c) is itself an exact solution of the ODE (3.3a). The general expansion for solutions of (3.3a) with the leading-order behavior at $\xi = d$ required by (3.3c) suggests a one-parameter (in addition to d) family of solutions and is given by

$$\varphi_0(\xi) = 2(2/3)^{1/2} (d - \xi)^{3/2} + a^+(d - \xi)^{3/2+\mu} + \sum_{n=2}^{\infty} a_n^+(d - \xi)^{3/2+\mu n}. \tag{3.5}$$

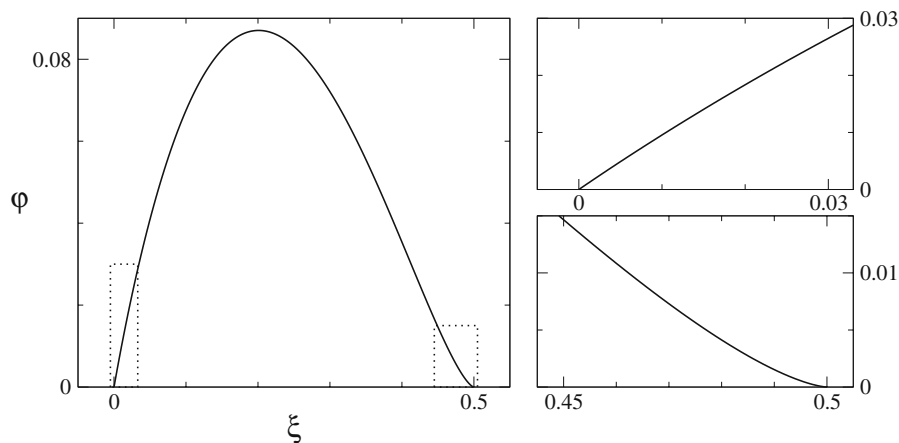


Fig. 2 The normalized base state for the base state of the slip model, obtained as numerical solution of (3.3)

Here, μ denotes the constant $\mu = (-1 + \sqrt{13})/4$ and a^+ is a free parameter. The coefficients a_n^+ must be determined recursively from the ODE for $n \geq 2$.

Similarly, at $\xi = 0$, we have a one-parameter family of solutions that satisfy the relevant boundary conditions (3.3b). In fact, in [37], Buckingham et al. find a general series expansion for (3.3a) at $\xi = 0$ that satisfies $h(0) = 0$ with two free parameters. Using the form given by the authors and enforcing the boundary conditions (3.3b) to fix one of the two free parameters, we obtain

$$\varphi_0(\xi) = \xi + (1/2)\xi^2 \log \xi + a^-\xi^2 + \sum_{n=3}^{\infty} \sum_{m=2}^n a_{nm}^-\xi^n (\log \xi)^{n-m} \quad \text{at } \xi = 0. \tag{3.6}$$

Here, a^- is the remaining free parameter, and the a_{mn}^- must be determined recursively from the ODE.

In summary, we have, for each boundary point, a two-dimensional invariant manifold of trajectories in the three-dimensional phase space of (3.3a). Solutions of (3.3) arise from intersections of these manifolds. These are co-dimension-one intersections, so that we expect a discrete family of solutions, for a discrete family of d . In fact, as pointed out by [33], upon integrating (3.3a) once and imposing the boundary conditions, one fixes the constant of integration and also obtain a single value for d :

$$d = \frac{1}{2}. \tag{3.7}$$

We solved this problem numerically, using LSODE [38], to solve (3.3a) with initial conditions obtained from the series expansion imposed at $\xi = \xi_1$ and $\xi = 1/2 - \xi_1$, with a small ξ_1 . Continuity of the solution and its derivative was imposed at the mid point $\xi = 1/4$ and these conditions solved numerically for a^- and a^+ by Newton iterations. We obtained $a^- = -2.175$ and $a^+ = -2.226$. The solution φ_0 is shown in Fig. 2.

4 Linear stability

4.1 Formulation

We first shift the governing equations of the sharp-interface model (2.34) to the moving frame of reference also used in (3.1), by letting $\bar{x} = x - ct$, and $\bar{s}^\pm = s^\pm - ct$, where now \bar{s}^\pm may be a non-constant function depending on y and t . After introducing the new variables, we drop the bars to give

$$h_t - ch_x + \nabla \cdot (h^2 \nabla \Delta h) = 0, \tag{4.1a}$$

$$h = 0, \quad \frac{h_x - h_y s_y^-}{(1 + (s_y^-)^2)^{1/2}} = \lambda, \quad h^2 \frac{\Delta h_x - \Delta h_y s_y^-}{(1 + (s_y^-)^2)^{1/2}} - \frac{(s_t^- + c) h}{(1 + (s_y^-)^2)^{1/2}} = 0, \quad \text{for } x = s_y^-, \tag{4.1b}$$

$$h \sim 2(2/3)^{1/2} \left(\frac{s_t^+ + c}{(1 + (s_y^+)^2)^{1/2}} \right)^{1/2} \left(\frac{s^+ - x}{(1 + (s_y^+)^2)^{1/2}} \right)^{3/2} \quad \text{as } x \rightarrow s^+. \tag{4.1c}$$

To address linear stability we now let

$$s^\pm \sim \pm s_0 + \beta s_1^\pm(t) e^{iky}, \quad h \sim h_0 + \beta h_1(x, t) e^{iky}, \tag{4.2}$$

where h_0, s_0^\pm denotes the solution of (3.1) obtained in the previous Sect. 3, which serves as our base state. To $O(\beta)$ we get

$$h_{1t} - ch_{1x} + \left[h_0^2 (h_{1xxx} - k^2 h_{1x}) \right]_x - k^2 h_0^2 (h_{1xx} - k^2 h_1) = 0 \tag{4.3}$$

with boundary conditions

$$h_1 + \lambda s_1^- = 0, \quad h_{1x} + h_{0xx} s_1^- = 0, \quad h_0^2 h_{1xxx} - ch_1 = 0 \tag{4.4a,b,c}$$

as $x \rightarrow s_0^-$ and

$$h_1 \sim 6^{1/2} c^{1/2} s_1^+ (s_0^+ - x)^{1/2} \tag{4.5}$$

as $x \rightarrow s_0^+$.

We make the ansatz

$$[s_1^\pm(t), h_1(x, t)] = [\hat{s}^\pm, \hat{h}(x)] e^{\alpha t} \tag{4.6}$$

and obtain from (4.3–4.5) and the variable transformation

$$x = \frac{\lambda^2}{c} \xi + s_0^-, \quad k = \frac{c}{\lambda^2} q, \tag{4.7a}$$

$$s_0^+ = \frac{\lambda^2}{2c} + s_0^-, \quad s_1^- = \frac{\lambda^2}{c} d_1^-, \quad s_1^+ = \frac{\lambda^2}{c} d_1^+, \tag{4.7b}$$

$$h_0 = \frac{\lambda^3}{c} \varphi_0, \quad h_1 = \frac{\lambda^3}{c} \varphi_1, \quad \alpha = \frac{c^2}{\lambda^2} \sigma, \tag{4.7c}$$

the eigenvalue problem

$$-\sigma \varphi_1 = \left(\varphi_0^2 \left(\varphi_{1\xi\xi} - q^2 \varphi_1 \right) \right)_\xi - q^2 \varphi_0^2 \left(\varphi_{1\xi\xi} - q^2 \varphi_1 \right) + \varphi_{1\xi}, \tag{4.8a}$$

$$\varphi_{1\xi} = \varphi_{0\xi\xi} \varphi_1, \quad \varphi_0^2 \varphi_{1\xi\xi\xi} - \varphi_1 = 0, \quad \text{at } \xi = 0, \tag{4.8b}$$

$$\varphi_1 \sim 6^{1/2} d_1^+ (1/2 - \xi)^{1/2} \quad \text{as } \xi \rightarrow 1/2, \tag{4.8c}$$

where φ_0 is the rescaled base state, i.e., the solution of (3.3). Note that we have used (4.4a), (4.4b) to eliminate s_1^- , i.e., d_1^- from (4.8b). Note also that the leading behavior of $\varphi_{0\xi\xi}$ in (4.8b) can be obtained by taking derivatives of (3.6),

$$\varphi_{0\xi\xi} = \frac{3}{2} + 2a^- + \log \xi + O(\xi \log \xi) \quad \text{for } \xi \rightarrow 0. \tag{4.9}$$

The general solution of the linear ODE (4.8a) can be found as a linear combination of four basis functions with the following distinct types of leading-order behavior,

$$\psi_1^- \sim 1 + o(\xi^2), \quad \psi_2^- \sim \xi + o(\xi^2), \quad \psi_3^- \sim \xi \log \xi + o(\xi^2), \quad \psi_4^- \sim \xi^2, \quad \text{as } \xi \rightarrow 0. \tag{4.10}$$

In view also of (4.9), a linear combination $h_1 = \sum_{i=1}^4 c_i \psi_i^-$ satisfies only (4.8b) if $c_3 = c_1$ and $c_2 = (1/2 + 2a^-) c_1$, i.e., in effect two conditions are imposed at the boundary $\xi = 0$. The general solution of the ODE that satisfies the boundary condition is then given by

$$\varphi_1 = c_1^- \phi_1^- + c_2^- \phi_2^-, \tag{4.11a}$$

where

$$\phi_1^- = 1 + \left(\frac{1}{2} + 2a^-\right) \xi + \xi \log \xi + O(\xi^2 \log \xi), \tag{4.11b}$$

$$\phi_2^- = \xi^2 + O(\xi^2 \log \xi), \tag{4.11c}$$

as $\xi \rightarrow 0$.

Similarly, the four possible leading-order behaviors as $\xi \rightarrow 1/2$ are given by $(1/2 - \xi)^\rho$ with $\rho = 0, 3/2 - \mu, 1/2$, and $1 + \mu$, where $\mu = (1 + \sqrt{13})/4$ denotes the same constant as in Sect. 3. Only the last two power-law behaviors are consistent with the boundary condition (4.8c), where the second last corresponds to a shift in location of the interface, i.e., we also effectively impose two conditions at the right boundary, yielding the total of four conditions required for a fourth-order eigenvalue problem. The general solution of (4.8a) that satisfies (4.8c) is given by

$$\varphi_1 = c_1^+ \phi_1^+ + c_2^+ \phi_2^+, \tag{4.12a}$$

where

$$\phi_1^+ \sim (1/2 - \xi)^{1/2}, \quad \phi_2^+ \sim (1/2 - \xi)^{(5+\sqrt{13})/4}. \tag{4.12b,c}$$

as $\xi \rightarrow 1/2$.

4.2 Numerical construction

To obtain the eigensolutions we use a construction based on the idea of Evans functions, [39–42]. For σ to be an eigenvalue, there must exist c_1^\pm and c_2^\pm so that $c_1^- \phi_1^- + c_2^- \phi_2^-$ and $c_1^+ \phi_1^+ + c_2^+ \phi_2^+$ are non-zero and equal for $0 \leq \xi \leq 1/2$. Then, the common function they represent is an eigenfunction corresponding to the eigenvalue σ . The two linear combinations are equal throughout the whole interval if their value and the first three derivatives are equal at an arbitrary point of the interval. Therefore, an eigenvalue is found if the Wronskian

$$W = \det A, \quad A = \begin{pmatrix} \phi_1^- & \phi_2^- & \phi_1^+ & \phi_2^+ \\ (\phi_1^-)' & (\phi_2^-)' & (\phi_1^+)' & (\phi_2^+)' \\ (\phi_1^-)'' & (\phi_2^-)'' & (\phi_1^+)'' & (\phi_2^+)'' \\ (\phi_1^-)''' & (\phi_2^-)''' & (\phi_1^+)''' & (\phi_2^+)''' \end{pmatrix}, \tag{4.13}$$

is zero at any point of the interval and hence everywhere. If this is the case, the kernel of A specifies the coefficients c_1^\pm and c_2^\pm that determine the eigenfunction via

$$A (c_1^-, c_2^-, -c_2^+, -c_1^+)^T = 0, \tag{4.14}$$

where the superscript indicates transposition.

We used this approach to obtain the eigenvalues and eigenfunctions numerically. For given q and a given candidate eigenvalue σ , we first computed the functions ϕ_1^\pm, ϕ_2^\pm using LSODE. The initial conditions for the numerical solver were imposed at ξ_2 and $1/2 - \xi_2$ for a small positive ξ_2 larger than the value ξ_1 for the base state: this was done to avoid the singular or near singular behavior at the boundary points and to obtain solutions with the prescribed leading behavior there. The initial conditions were obtained from the first few terms of the series expansions of each of the four solutions, which were determined prior to the numerical computations with the aid of MAPLE. At $\xi = 1/4$, we computed the Wronskian. We restricted our attention to real eigenvalues so that the value of σ for which W vanishes could be determined by bisectioning.

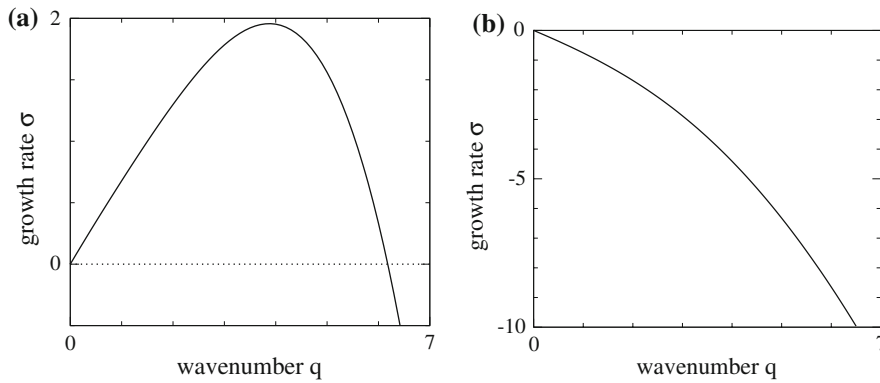


Fig. 3 The top eigenvalue ((a), left figure) and the bottom eigenvalue ((b), right figure) in the slip dominated case, i.e., for (4.8)

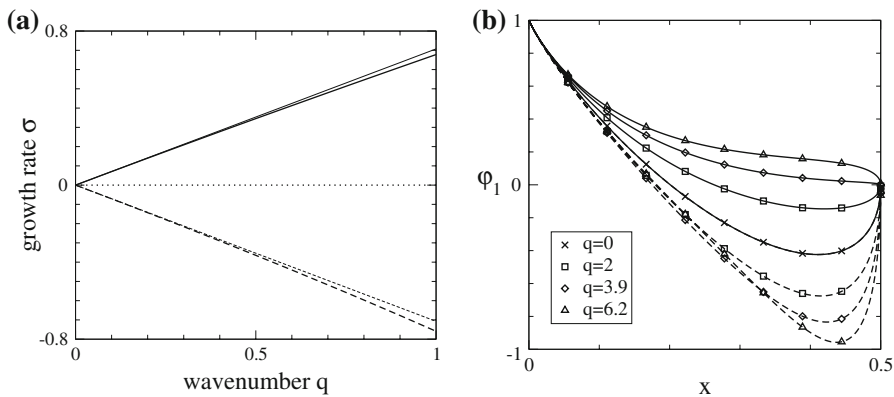


Fig. 4 (a) A zoom into the long-wave range (small q) range for the top and bottom eigenvalues. The thicker lines are numerical results for the eigenvalue problem (4.8), the thinner ones come from the long-wave approximation (4.23b). (b) The eigenfunctions for both eigenvalues for a number of different wavenumbers q . Solid lines are used for the eigenfunctions of the top, and dashed lines for those of the bottom, eigenvalue, respectively. The symbols indicate the corresponding value of q . For $q \rightarrow 0$, the two lines coincide since both eigenfunctions tend to the translational mode (i.e., to $\varphi_{0,\xi}$)

We found two eigenvalues, shown in Fig. 3. The “top” eigenvalue is positive for a range of $q > 0$ up to a cut-off wave number $q_c = 6.18$ and has a distinct maximum at $q = q_m = 3.88$, which determines a preferred wave-length for the instability. The other, or “bottom” eigenvalue is always stable. Both eigenvalues tend to zero for $q \rightarrow 0$. The corresponding eigenfunctions are shown in Fig. 4. Since eigenfunctions can be rescaled with an arbitrary factor, we can enforce a normalisation condition, which here we chose to be

$$\varphi_1 = 1 \text{ at } \xi = 0. \tag{4.15}$$

Interestingly, for $q \rightarrow 0$, the eigenfunctions for the two eigenvalues both tend to the translational mode $\varphi_{0\xi}$. This is in contrast to the situation for the static ridge where the eigenfunctions tend to two different eigenfunctions for $q \rightarrow 0$, namely the peristaltic mode and the varicose mode. Inspection of the solutions of (4.8) for $\sigma = 0$ and $q = 0$ shows that, while the translational mode $\varphi_{0\xi}$ is an eigenfunction for $\sigma = 0$ where $q = 0$, the variation of the base state with respect to rescaling is $\xi\varphi_{0\xi} - \varphi_0$, which is only a generalized eigenfunction, in the sense that plugging it into (4.8a) yields the eigenfunction.

Furthermore, the behavior of $\sigma(q)$ is linear in q for $q \rightarrow 0$ for both eigenvalues, i.e., $\sigma(q) \sim \sigma_1|q|$ rather than the $O(q^2)$ leading-order behavior that is typically observed for the finger instability in, e.g., gravity- or Marangoni-driven thin-film flows. But see also [43], where, via different arguments, similar behavior was found for the situation of sliding two-dimensional droplets, or [44], where the stability of a spreading surfactant-laden droplet is analysed.

4.3 The long-wave limit

A long-wave expansion that we carry out now reveals that this behavior is due to the fact that for $q = 0$, the double eigenvalue $\sigma = 0$ has one proper and one generalized eigenfunction, i.e., the long-wave expansion arises as the perturbation of an algebraically double eigenvalue of geometric multiplicity one. We first define L to be the linear differential operator that describes the left-hand side of (4.8a), i.e.,

$$L\varphi_1 \equiv \left(\varphi_0^2 \left(\varphi_{1\xi\xi} - q^2\varphi_1 \right) \right)_\xi - q^2\varphi_0^2 \left(\varphi_{1\xi\xi} - q^2\varphi_1 \right) + \varphi_{1\xi}.$$

Furthermore, let L_0 and L_1 be the parts of L that correspond to terms that are, respectively, independent of and quadratic in q . Also, let L_0^* denote the adjoint operator of L_0 :

$$L_0\varphi \equiv \left(\varphi_0^2 \varphi_{\xi\xi\xi} \right)_\xi + \varphi_{\xi\xi}, \quad L_1\varphi \equiv - \left(\varphi_0^2 \varphi_{\xi\xi} \right)_\xi - \varphi_0^2 \varphi_{\xi\xi\xi}, \quad L_0^*\psi \equiv \left(\varphi_0^2 \psi_\xi \right)_{\xi\xi\xi} - \psi_{\xi\xi}. \tag{4.16a,b,c}$$

We seek an expansion for the eigenvalues and eigenfunctions σ and φ_1 of (4.8) of interest in terms of q . Motivated by our numerical findings, we make the ansatz (assuming $q \geq 0$):

$$\sigma = \sigma_1 q + \sigma_2 q^2 + O(q^3), \quad \varphi_1 = \varphi_{0\xi} + \varphi_{11} q + \varphi_{12} q^2 + O(q^3). \tag{4.17}$$

Plugging this ansatz and the expansions of L in (4.16) into $L\varphi_1 = -\sigma\varphi_1$, the leading-order terms are zero, while for the $O(q)$ and $O(q^2)$ problems we obtain

$$L_0\varphi_{11} = -\sigma_1\varphi_{0\xi}, \quad L_0\varphi_{12} + L_1\varphi_{0\xi} = -\sigma_1\varphi_{11} - \sigma_2\varphi_{0\xi}. \tag{4.18a,b}$$

Also, we continue to enforce the normalisation condition (4.15) on φ_1 , which implies

$$\varphi_{1l} = 0 \quad \text{at } \xi = 0 \quad \text{for } l \geq 1. \tag{4.19}$$

Equation (4.18a) implies that φ_{11} must be the σ_1 multiple of the generalized eigenfunction $\bar{\rho}$, plus an arbitrary multiple of ρ . The arbitrariness is removed by (4.19), and we obtain

$$\varphi_{11} = -\sigma_1 (\xi\varphi_{0\xi} - \varphi_0). \tag{4.20}$$

We plug this result into (4.18b) and integrate the equation with respect to ξ , which yields,

$$\int_0^{1/2} L_1\varphi_{0\xi} \, d\xi = \sigma_1^2 \int_0^{1/2} \xi\varphi_{0\xi} - \varphi_0 \, d\xi. \tag{4.21}$$

The integrals on both sides can be evaluated by partial integration, and then we can solve for $\sigma_1^2 = 1/2$, or

$$\sigma_1 = \pm \frac{\sqrt{2}}{2}. \tag{4.22}$$

Together with (4.20) we therefore obtain to $O(q)$ for the branches of eigensolution

$$\sigma = \pm \frac{\sqrt{2}}{2} q, \quad \varphi_1 = \varphi_{0\xi} \mp \frac{\sqrt{2}}{2} q (\xi\varphi_{0\xi} - \varphi_0). \tag{4.23a,b}$$

The knowledge of the eigenfunctions can be used to determine how the unstable mode perturbs the two boundaries. For a given eigenfunction h_1 for an unstable eigenvalue σ for some q , the left boundary is perturbed by $d_1^- e^{iqy+\sigma t}$, where $d_1^- = -\varphi_1(0)$. This follows from (4.4a), rescaled by (4.7). On the other hand, it follows from (4.8c) that $d_1^+ e^{iqy+\sigma t}$ is the perturbation of the right boundary, and

$$d_1^+ = \lim_{\xi \rightarrow 1/2} \left[\varphi_1 / 6^{1/2} (1/2 - \xi)^{1/2} \right].$$

Since the eigenfunction φ_1 is given as a linear combination of the functions ϕ_1^\pm and ϕ_2^\pm , the expansions of which we know at the boundaries, the values of d_1^\pm can be expressed in terms of c_1^\pm and c_2^\pm . One finds $d_1^- = -c_1^-$ and $d_1^+ = c_1^+ / 6^{1/2}$, thus

$$d_{\text{rel}} \equiv \frac{d_1^+}{d_1^-} = \frac{c_1^+ / 6^{1/2}}{-c_1^-}. \tag{4.24}$$

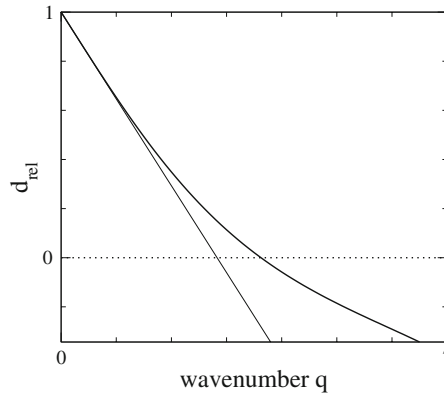


Fig. 5 The perturbation of the right boundary relative to the perturbation of the left boundary, obtained from the eigenfunction for the top eigenvalue via (4.24), for a range of different wave numbers q . The thicker, curved line is obtained by evaluating (4.24) using the numerically computed eigenfunctions, while the thinner line uses the long-wave approximation, i.e., the formula given in (4.25). Further explanations are given in the text

For the translation mode, both boundaries are shifted by the same amount in the same direction, and therefore $d_{rel} = 1$. The graphs of the eigenfunctions in Fig. 3 suggest that the contribution of ϕ_1^+ hence c_1^+ decreases as q increases and eventually changes sign. This is indeed the case, as seen in Fig. 5, where the d_{rel} is shown as a function of q . The function decreases monotonically from one and crosses zero near $q = 3.62$, just below the preferred wavenumber q_m .

For $q > 3.62$, the perturbation of the right boundary is out of phase with the left boundary by half a period, so that rim would be composed by thinner and thicker parts resembling a peristaltic perturbation. However, near $q = 3.62$ the perturbation of the right boundary is nearly zero and even when q approaches the cut-off wavenumber q_c , beyond which the perturbation decays anyway, d_{rel} is less than 0.4, i.e., the perturbation is less than half the size of the left boundary. Hence, all unstable perturbations will appear to be ‘asymmetric’ in the sense that the side facing the undisturbed film is much less perturbed than the side facing the dewetted area.

The expression (4.24) can be obtained approximately using the long-wave approximation for the eigenfunction (4.23b), and this leads to

$$d_{rel} = 1 - \frac{\sqrt{2}}{4}q + O(q^2). \tag{4.25}$$

The corresponding straight line is also shown in Fig. 5 as a thinner line. It compares well with the numerical result for small and even moderate values of q .

5 Comparison to the full lubrication model

As a next step, we investigate the stability of a growing rim for the full lubrication model in the slip case, given by (2.4), (2.5).

First, we obtain the base state by solving these equations numerically for the case where h does not depend on y , using a slightly smoothed jump as initial data. We use here $\epsilon = 0.04$ and set $\beta = 1$, as well as a slightly modified intermolecular potential

$$\Phi(h) = \Phi_2(h) \equiv \frac{a_1}{8h^8} - \frac{a_2}{2h^2} + \frac{a_3}{2(h+d)^2}, \tag{5.1a}$$

with

$$a_1 = 1.014, \quad a_2 = 1.014, \quad a_3 = 7.465, \quad d = 25.34. \tag{5.1b}$$

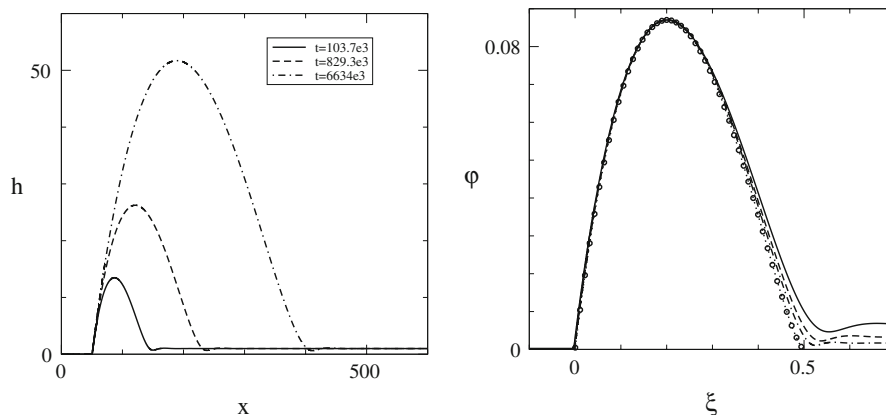


Fig. 6 (a) Evolution of the dewetting rim profile obtained by solving (2.4), (2.5) (for only one spatial variable x), with $\epsilon = 0.04$ and $\beta = 1$. The potential is given by (5.1). The figure shows the rim at three different times t . (b) The same rim profiles rescaled as explained in the text; see (5.2), using the same line styles as on the left. The fourth profile, shown by open circles, corresponds to the solutions φ for the sharp-interface model; see also Fig. 2

This three-term potential was motivated by numerical studies in earlier articles [23, 24, 34].

The base profile grows as the rim moves in the direction of the unperturbed film; see Fig. 6(a). From the scalings in (3.2) we see that the growth of the height and width of the rim is inversely proportional to the dewetting rate $c = \dot{s}$. Thus, the dewetting rate decreases as the rim moves further into the unperturbed film. In fact, a specific law for the evolution of the contact-line region, $s(t) \sim t^{2/3}$, can be found from the rescalings (3.2) and a mass-balance argument. Derivations and discussions of this law can be found in the literature [24, 33, 45–47].

The rescalings (3.2) of the traveling-wave solution in Sect. 3 lead to a universal profile φ_0 without any free parameters. Hence, if we rescale the profiles in Fig. 6(a) that were obtained for the full lubrication model according to (3.2), we expect the result to closely approximate φ_0 . Instead of obtaining c from the evolution of the contact line, we rescale h by $\max_x(h(x, t))/\max_\xi(\varphi_0(\xi))$; the corresponding lateral length-scale is found by comparison with (3.2). Hence, we rescale according to

$$h = \frac{\max_x(h(x, t))}{\max_\xi(\varphi_0(\xi))} \hat{\varphi}, \quad x = \frac{\max_x(h(x, t))}{\lambda \max_\xi(\varphi_0(\xi))} \xi. \tag{5.2}$$

The result is shown in Fig. 6(b). We clearly see that the rescaled solutions of the full lubrication model converge, for later times, onto the normalized traveling solution φ for the sharp-interface model, i.e., of (3.3). This is to be expected since, for later times, the rim is larger and hence the residual film and the unperturbed film thickness are smaller relative to the rim height, and this means the effective ϵ and β are smaller.

As next step we describe the occurrence of fingers in the ridge for the full lubrication model in terms of the evolution of a small perturbation of the base state which we now denote by $h_b(x, t)$. Specifically, we introduce the perturbation

$$h(x, y, t) = h_b(x, t) + \delta h_p(x, t) \exp(iky)$$

into the lubrication model, with $\delta \ll 1$ and retain only linear terms in δ . We obtain for the linearized equation

$$\frac{\partial h_p}{\partial t} + \mathcal{L}h_p - k^2 \left[\left(h_b^2 h_{1x} \right)_x + h_b^2 \left(h_{1xx} - \epsilon^{-2} \Phi''(h_b/\epsilon) \right) \right] + k^4 h_b^2 h_p = 0, \tag{5.3}$$

where

$$\begin{aligned} \mathcal{L}h_p \equiv & \frac{\partial}{\partial x} \left[2h_b^2 \left(h_{bxx} - \epsilon^{-2} \Phi''(h_b/\epsilon) \right) h_p - h_b^2 \epsilon^{-2} \Phi''(h_b/\epsilon) h_{bx} h_p \right. \\ & \left. + h_b^2 \left(h_{1xxx} - \epsilon^{-2} \Phi''(h_b/\epsilon) h_{1x} \right) \right]. \end{aligned} \tag{5.4}$$

Note that, since we have a time-dependent base state, the coefficients of the linearized PDE are non-constant in time; hence solutions for the linearized problem cannot be obtained via a classical eigenvalue approach. Instead, we numerically solve an initial-value problem for (5.3), (5.4) for a fixed set of wavenumbers, in tandem with the equation for the base state, and observe how the perturbations evolve in time. The computational effort scales roughly linearly with the number of wave-numbers we monitor.

The evolution is computed for a time interval $[t_0, t_1]$ where t_0 and t_1 are the times where the unperturbed front, more specifically, the left contact-line regions, estimated for the purpose of this subsection by the position of the turning point, has reached a certain position, namely

$$s(t_0) = 0.883 \quad \text{and} \quad s(t_1) = 1.48 \times 10^4;$$

the corresponding times are

$$t_0 = 5.18 \quad \text{and} \quad t_1 = 9.85 \times 10^6.$$

An initial perturbation $h(t)$ is introduced at time t_0 using the following expression:

$$h_p(x, t_0) = \frac{\partial h_b}{\partial x}(x, t_0), \tag{5.5}$$

which corresponds to a ‘zig-zag’ perturbation, i.e., we perturb both sides of the ridge in the same direction [48]. For zero wave-number, Eq. 5.5 simply represents an infinitesimal initial shift of the whole profile. Below, we also make some remarks on other choices of the initial data for h_p .

To describe the growth of bumps and eventually fingers in the ridges, we use the amplification $A(t)$ of the perturbation with respect to the initial state,

$$A(t) \equiv \frac{\max_x |h_p(x, t)|}{\max_x |h_p(x, t_0)|} \quad \text{for} \quad t_0 \leq t \leq t_1.$$

We compare amplifications achieved at the same position of the dewetting fronts, rather than at the same value of t . Figure 7 displays $A(t)$ vs. the front position $s(t)$ for several wavelengths $l = 2\pi/k$. For each of the depicted wavelengths, the perturbation grows as the dewetting proceeds, then it reaches a maximum, after which it decays. Longer wavelengths achieve the maximal amplification factor

$$A_{\max} \equiv \max_{t \geq t_0} A(t)$$

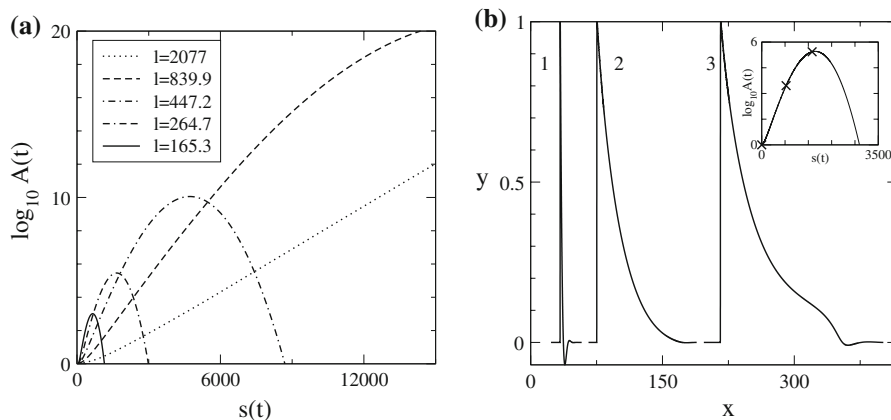


Fig. 7 (a) Amplification $A(t)$ of the perturbation versus front position $s(t)$. Line styles correspond to different wavelengths $l = 2\pi/k$ as indicated in the legend. (b) The perturbation profile for wavelength $l = 264.7$ at different stages of its evolution, shifted along the x -axis for better distinction, and with the maximum normalized to one. The labels 1, 2, 3 correspond to the crosses in the inset, which indicate the position $s(t)$ of the base state and the amplification $A(t)$ achieved by $h_p(x, t)$

at later stages of the dewetting, when the front has advanced further into the film and the ridge of the base state has grown in size, suggesting that the most amplified wavelength correlates with the width of the ridge [22]. This coincides interestingly with results on the fingering in gravity and Marangoni-driven flows, where the most amplified wavelength in the modal analysis is proportional to the length-scale imposed by the bump width [4], and with predictions for the breaking up of static ridges [48] into droplets.

Figure 7(b) shows profiles of the perturbation h_b for a fixed choice of $k = 0.0237$ at different stages of amplification. The initial perturbation (given by (5.5)), which has one pronounced maximum and a minimum, slowly evolves into a new profile where the minimum is replaced by a relatively flat part with a weak tendency to create a second ‘bump’ in the profile of the perturbation after the maximum amplification has been achieved. This clearly resembles observations made earlier for the eigenfunctions of the linearized sharp-interface model.

In fact, we can compare the shape of the perturbation with the eigenfunction in a similar way as before for the base state. We rescale x into ξ as in the second part of (5.2), leaving h_p normalized so that the maximum is one. Also, we need to determine the wavenumber for which to take the eigenfunction of the linearized sharp-interface model. This is found by scaling k with the inverse of the scale for x ,

$$k = \frac{\lambda \max_{\xi}(\varphi_0(\xi))}{\max_x(h(x, t))}q. \tag{5.6}$$

For the h_p -profile labelled ‘2’ in Fig. 7(b), we obtain $q = 6.02$ which is very close to the cut-off wavenumber for the sharp-interface model. Note that since $\max_x(h(x, t))$ increases with time, the ‘‘effective’’ wavenumber q decreases with time, and in fact, at the time t_{\max} when $A(t)$ reaches its maximum value A_{\max} , which is slightly after the time of profile ‘2’, the value for q turns out to approximate the cut-off wavenumber very closely.

In Fig. 8, we now compare the rescaled h_p -profile with the eigenfunction of (4.8) for $q = 6.02$. We see good agreement for $\xi < 0.2$ but some deterioration as ξ approaches $1/2$. In general, however, we can expect the agreement to improve if we start with a larger $l = 2\pi/k$, since then the base profiles are larger when a certain value of q is reached, hence the thickness of the residual and the unperturbed film thickness are smaller compared to the size of the rim.

Furthermore, note that the evolution of the base state $h_b(x, t)$ is algebraic and thus slow compared to the rapid exponential growth of an unstable mode of (4.3). This suggests that the evolution of h_p is given at every instance by solving (4.3) for the most unstable mode. This means in particular that we treat $c = \dot{s}(t)$ as a constant for the purpose of solving (4.3), but retain its slow algebraic growth in the solution itself, in the sense of a ‘‘quasistatic’’ approximation. This yields

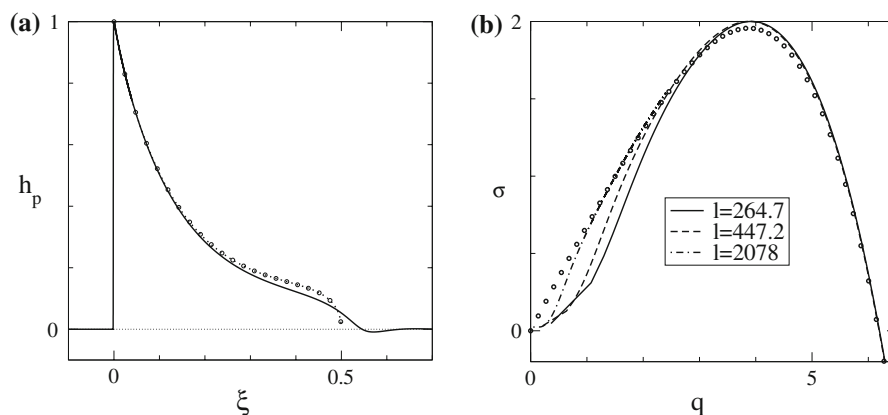


Fig. 8 (a) Comparison of the rescaled perturbation $h_p(x, t)$ labelled ‘2’ (solid line) with the eigenfunction of the sharp-interface model for the corresponding wavenumber q (circles). (b) Comparison of the rescaled growth rates $\hat{\sigma}$ and wavenumbers q obtained from the solutions h_p for several choices of fixed $l = 2\pi/k$, with the dispersion relation for the sharp-interface model (circles). Further explanations for (a) and (b) are given in the text

$$h_1(x, t) = \frac{\lambda^3}{c} \varphi_1(\xi; q) \exp\left[\frac{c^2}{\lambda^2} \sigma t\right], \quad \xi = \frac{c}{\lambda^2}(x - s), \quad q = \frac{\lambda^2}{c}k, \tag{5.7}$$

where φ_1 and σ represent the eigensolution of (4.8) with the largest real part of σ . Recall that since the wave number k of the perturbation of the full lubrication model is kept fixed, q now changes due to the quasi-static evolution of $c = c(t) = \dot{s}$.

Rather than comparing (5.7) directly with h_p we solve (5.7) to express σ in terms of a normalized maximum of h_1 ,

$$\sigma = \frac{\lambda^2}{c^2} \frac{d}{dt} \log\left[\frac{\max_x h_1(x, t)}{\max_x h_1(x, t_0)}\right] \tag{5.8}$$

and then replace h_1 by h_p , i.e., we monitor

$$\hat{\sigma} = \hat{\sigma}(t) = \frac{\lambda^2}{c^2} \frac{d}{dt} \log A(t; k). \tag{5.9}$$

The expression $\hat{\sigma}$ can be evaluated in time using the numerical solutions for h_p for an arbitrary fixed choice of k . We note that it is convenient to avoid determining $c(t) = \dot{s}(t)$, so we proceed as for the rescaling of the base state and use (5.2), (5.6). The corresponding time-scale can be found by comparison with (3.2), so that we actually compute $\hat{\sigma}$ via

$$\hat{\sigma} = \left[\frac{\max_x(h(x, t))}{\lambda^2 \max_\xi(\varphi_0(\xi))}\right]^2 \frac{d}{dt} \log A(t; k) \tag{5.10}$$

to generate the lines in Fig. 8(b).

If h_p is indeed well approximated by h_1 , then the dispersion relation $(q, \sigma(q))$ obtained from the eigenproblem (4.8) must be well approximated by the curve $(q(t), \hat{\sigma}(t))$. In fact, we can argue similarly as before that $(q(t), \hat{\sigma}(t))$ is expected to asymptotically approach $(q, \sigma(q))$ as we consider larger t for the same fixed k , which means larger $q(t)$ or repeat the procedure with a larger choice for k . Indeed, this is what we see in Fig. 8(b).

6 Conclusion

In this paper we have studied the finger instability of thin polymer-film dewetting from a hydrophobic substrate. The appropriate *intermediate-slip* lubrication that describes the dynamics and morphology of the evolving film for large slip lengths has been derived in [24]. Its stability properties has been addressed in [23]. However, it turned out that the stability analysis of the full lubrication model must take into account a time-dependent base state, due to the growing rim of the dewetting film. This makes parameter studies and a derivation of the most preferred wavelength more difficult and numerically time-consuming.

We have found that we can make use of the slow growth of the rim compared to the faster time-scale on which the instability evolves as well the large height of the rim compared to the small heights of the adjacent undisturbed and the remaining film. Using matched asymptotic expansions we derived the sharp-interface model for a dewetting rim from the corresponding intermediate-slip lubrication model. In this reduced model all information on the evolving regions adjacent to the rim is now contained in the boundary conditions derived via matching. In particular, the base state is now stationary in an appropriate co-moving reference frame, thus enabling a stability analysis of the linearized problem for the rim via eigenvalue analysis. In this way, we have overcome the difficulties of the stability problem for the original intermediate-slip lubrication model which has a time-dependent base state.

Interestingly, the resulting sharp-interface model for which we derived analytical expressions for the dispersion relations show that the dependence of the growth rate on the wavenumber is linear for small wavenumbers. This is in contrast to the quadratic dependence typically found for finger-type instabilities in thin-film problems, such as for gravity or Marangoni-driven film flows.

We presently are in the process to derive a sharp-interface model for the no-slip case to study its stability properties, dispersion relations etc., and expect to show quadratic dependence of the growth rate on the wavenumber. This will be the topic of a companion paper to follow.

With these studies we hope to shed some light on the mechanisms that underlie and determine the wavelengths that are actually seen in the experiments. Additionally, a comparison of our results with experiments that can accurately determine an effective wavelength, i.e., the destabilizing wavelength over the width of the rim, is underway.

Acknowledgements AM gratefully acknowledges support by a Heisenberg fellowship. AM and BW are grateful for the support by the DFG research center MATHEON in Berlin and by the DFG Priority Programme *Nano- and Microfluidics*. JRK gratefully acknowledges the support of the Royal Society/Wolfson foundation.

References

- Bertozzi AL, Brenner MP (1997) Linear stability and transient growth in driven contact lines. *Phys Fluids* 9:530–539
- Huppert H (1982) Flow and instability of a viscous current down a slope. *Nature* 300:427–429
- Silvi N, Dussan EBV (1985) On the rewetting of an inclined solid surface by a liquid. *Phys Fluids* 28:5–7
- Troian SM, Herbolzheimer E, Safran SA, Joanny JF (1989) Fingering instabilities of driven spreading films. *Europhys Lett* 10:25–30
- Bertozzi AL, Münch A, Fanton X, Cazabat AM (1998) Contact line stability and ‘undercompressive shocks’ in driven thin film flow. *Phys Rev Lett* 81:5169–5172
- Brzoska JB, Brochard-Wyart F, Rondelez FB (1992) Exponential growth of fingering instabilities of spreading films under horizontal thermal gradients. *Europhys Lett* 19:97–102
- Cazabat AM, Heslot F, Troian SM, Carles P (1990) Finger instability of thin spreading films driven by temperature gradients. *Nature* 346(6287):824–826
- Garnier N, Grigoriev RO, Schatz MF (2003) Optical manipulation of microscale fluid flow. *Phys Rev Lett* 91:054501
- Kataoka DE, Troian SM (1997) A theoretical study of instabilities at the advancing front of thermally driven coating films. *J Coll Int Sci* 192:350–362
- López PG, Bankoff SG, Miksis MJ (1996) Non-isothermal spreading of a thin liquid film on an inclined plane. *J Fluid Mech* 11:1–39
- Münch A, Wagner BA (1999) Numerical and asymptotic results on the linear stability of a thin film spreading down a slope of small inclination. *Euro J Appl Math* 10:297–318
- Seemann R, Herminghaus S, Jacobs K (2001) Dewetting patterns and molecular forces: A reconciliation. *Phys Rev Lett* 86:5534–5537
- Seemann R, Herminghaus S, Jacobs K (2001) Gaining control of pattern formation of dewetting films. *J Phys C* 13:4925–4938
- Konnur R, Kargupta K, Sharma A (2000) Instability and morphology of thin liquid films on chemically heterogeneous substrates. *Phys Rev Lett* 84:931–934
- Neto C, Jacobs K (2004) Dynamics of hole growth in dewetting polystyrene films. *Physica A* 339:66–71
- Reiter G (1992) Dewetting of thin polymer films. *Phys Rev Lett* 68:75–78
- Reiter G, Sharma A, Casoli A, David M-O, Khanna R, Auroy P (1999) Thin film instability induced by long-range forces. *Langmuir* 15:2551–2558
- Sharma A, Khanna R (1998) Pattern formation in unstable thin liquid films. *Phys Rev Lett* 81(16):3463–3466
- Sharma A, Khanna R (1999) Pattern formation in unstable thin liquid films under influence of antagonistic short- and long-range forces. *J Chem Phys* 110(10):4929–4936
- Xie R, Karim A, Douglas JF, Han CC, Weiss RA (1998) Spinodal dewetting of thin polymer films. *Phys Rev Lett* 81:1251–1254
- Lauga E, Brenner MP, Stone HA (2007) The no-slip boundary condition. In: Tropea C, Yarin A, Foss JF (eds) *Handbook of experimental fluid dynamics*. Springer, Heidelberg
- Masson J-L, Olufokunbi O, Green PF (2002) Flow instabilities in entangled polymer films. *Macromolecules* 35:6992–6996
- Münch A, Wagner B (2005) Contact-line instability of dewetting thin films. *Physica D* 209:178–190
- Münch A, Wagner BA, Witelski TP (2006) Lubrication models with small to large slip lengths. *J Eng Math* 53:359–383
- Reiter G, Sharma A (2001) Auto-optimization of dewetting rates by rim instabilities in slipping polymer films. *Phys Rev Lett* 80:166103
- Sharma A, Reiter G (1996) Instability of thin polymer films on coated substrates: rupture, dewetting and drop formation. *J Colloid Interface Sci* 178:383–389
- Brenner MP, Gueyffier D (1999) On the bursting of viscous films. *Phys Fluids* 11(3):737–739
- Eggers J (1997) Nonlinear dynamics and breakup of free-surface flows. *Rev Mod Phys* 69:865–929
- Münch A (2005) Dewetting rates of thin liquid films. *J Phys C* 17:309–318
- Brochard-Wyart F, de Gennes P-G, Hervert H, Redon C (1994) Wetting and slippage of polymer melts on semi-ideal surfaces. *Langmuir* 10:1566–1572
- Jacobs K, Seemann R, Schatz G, Herminghaus S (1998) Growth of holes in liquid films with partial slippage. *Langmuir* 14:4961–4963
- Redon C, Brochard-Wyart F, Rondelez F (1991) Dynamics of dewetting. *Phys Rev Lett* 66:715–718
- Flitton JC, King JR (2005) Surface-tension-driven dewetting of Newtonian and power-law fluids. *J Eng Math* 50:241–266

34. Münch A (2004) Fingering instability in dewetting films induced by slippage. MATHEON Preprint number 123
35. King JR, Münch A, Wagner BA (2006) Linear stability of a ridge. *Nonlinearity* 19:2813–2831
36. Tuck EO, Schwartz LW (1990) A numerical and asymptotic study of some third-order ordinary differential equations relevant to draining and coating flows. *SIAM Rev* 32:453–469
37. Buckingham R, Shearer M, Bertozzi A (2003) Thin film traveling waves and the Navier-slip condition. *SIAM J Appl Math* 63:722–744
38. Hindmarsh AC (1983) ODEPACK, a systematized collection of ODE solvers. In: Stepleman RS et al (eds) *Scientific computing, vol 1 of IMACS transactions on scientific computation*. North-Holland, Amsterdam, pp 55–64.
39. Evans JW (1972) Nerve axon equations: I. *Ind Univ Math J* 21:877–885
40. Evans JW (1972) Nerve axon equations: II. *Ind Univ Math J* 22:75–90
41. Evans JW (1972) Nerve axon equations: III. *Ind Univ Math J* 22:577–593
42. Evans JW (1975) Nerve axon equations: IV. *Ind Univ Math J* 24:1169–1190
43. Thiele U, Knobloch E (2003) Front and back instability of a liquid film on a slightly inclined plane. *Phys Fluids* 15:892–907
44. Jensen OE, Naire S (2006) The spreading and stability of a surfactant-laden drop on a prewetted substrate. *J Fluid Mech* 554:5–24
45. Brochard-Wyart F, Debregeas G, Fondécave R, Martin P (1997) Dewetting of supported viscoelastic polymer films: Birth of rims. *Macromolecules* 30:1211
46. Redon C, Brzoska JB, Brochard-Wyart F (1994) Dewetting and slippage of microscopic polymer films. *Macromolecules* 27:468–471
47. Reiter G, Khanna R (2000) Kinetics of autophobic dewetting of polymer films. *Langmuir* 16:6351–6357
48. Brochard-Wyart F, Redon C (1992) Dynamics of liquid rim instabilities. *Langmuir* 8:2324–2329